DRAFT VERSION MAY 26, 2020
Preprint typeset using LaTeX style emulateapj v. 01/23/15

MILKY WAY TOMOGRAPHY WITH THE SKYMAPPER SOUTHERN SURVEY: II: PHOTOMETRIC CALIBRATIONS FOR THE SECOND DATA RELEASE OF THE SKYMAPPER SOUTHERN SURVEY

Y. HUANG[1], H.-B. YUAN[2], C.-Y. LI[3,4], C. WOLF[5], C. ONKEN[6], T. BEERS[6,7], B.-Q. CHEN[1], AND X.-W. LIU[1]

Draft version May 26, 2020

ABSTRACT

In this paper, we apply the spectroscopy-based stellar color regression (SCR) method proposed by Yuan et al. to perform accurate photometric calibration for the second data release of the SkyMapper Southern Survey (SMSS DR2). By using a total number of over 200,000 dwarf stars with stellar atmospheric parameters taken from the GALAH DR3 and with homogeneous accurate photometry from the Gaia DR2, strong reddening dependent zero-point (ZP) errors are detected in the photometric catalog of SMSS DR2. The ZP errors are nearly zero at nil extinction and then steadily increase with $E(B-V)$, and can reach as large as 0.24, 0.23, 0.03, 0.02, 0.04, 0.05 mag in $uvgriz$ bands, respectively, at $E(B-V) \sim 0.5$. The errors are largely from the dust term in the transformations used by SMSS DR2 to construct photometric calibrators from the Pan-STARRS1 (PS1) photometry. Our study also reveals small but significant spatial variations of the ZP errors in all six bands. By properly correcting for the reddening and spatial dependent systematics, final ZP accuracies of 6.7, 5.7, 2.1, 2.5, 1.5 and 1.6 mmag at $uvgriz$ bands have been achieved for 50 per cent calibrated fields by our SCR technique.

Keywords: Galaxy: stellar content – stars: fundamental parameters – stars: distances – methods: data analysis

1. INTRODUCTION

Our knowledge about the Milky Way (MW) and the large-scale structure of the universe has been revolutionized by the wield-field large and systematic optical and near-infrared digital imaging sky surveys, such as the Sloan Digital Sky Survey (SDSS; York et al. 2000), the Two Micron All Sky Survey (2MASS; Skrutskie et al. 2006), the Wide-field Infrared Survey Explorer (WISE; Wright et al. 2010); the Pan-STARRS1 surveys (PS1; Chambers et al. 2016), the SkyMapper Southern Survey (SMSS; Wolf et al. 2018), the Dark Energy Survey (DES; DES Collaboration 2016) and the Gaia survey (Gaia Collaboration et al. 2016, 2018). It is heartening that more and more next-generation wield-field imaging surveys are in full swing, like the Large Synoptic Survey Telescope (LSST; Ivezić et al. 2019), the Javalambre Physics of the Accelerating Universe Astrophysical Survey (J-PAS; Benitez et al. 2014); and the Multi-channel Photometric Survey Telescope (Mephisto; Er et al. 2020).

Homogeneous and accurate photometric calibration is the most important step of the above surveys to translate the observed signals to the absolute physical flux scale (on top of the earth atmosphere). The accurate colors and magnitudes are required to provide robust classifications, photometric redshift estimates of a large number of galaxies to further explore the large-structure of the universe (e.g., Padmanabhan et al. 2007; Abbott et al. 2019), and to derive the stellar basic properties (e.g., effective temperature, metallicity, age and luminosity) of a huge number of stars to probe the Galactic structure (e.g., Jurić et al. 2008; Ivezić et al. 2008; Huang et al. 2019). To fulfill these ambitious scientific aims, photometric calibration of ≤ 1 per cent accuracy is challenging for the current and future large-scale photometric surveys.

The traditional optical photometric calibration is based on the networks of standard stars with flux well determined (e.g., Landolt 1992, 2009, 2013; Stetson 2000). However, achieving ≤ 1 per cent accuracy by using the traditional technique for ground-based large-scale photometric surveys is a difficult mission since 1) significant systematic errors would be induced when converting photometric system of the standards to the one you are concerned (e.g., Padmanabhan et al. 2008; Finkbeiner et al. 2016); 2) the spatial and temporal variations of Earth atmospheric transmission and instrumental effects are hard to be monitored by the traditional approach (e.g., Stubbs & Tonry 2006; Yuan et al. 2015).

Thanks to the successful implementations of the large-scale digital sky surveys, especially the SDSS survey, in the past decades, several different methods have been developed to pursue the ≤ 1 per cent accuracy for photometric calibrations across a large sky area. One main method is the ubercalibration first developed for the SDSS survey (Padmanabhan et al. 2008). This method first achieves uniform internal calibrations using the overlapping observed regions and the photometric zero-point (ZP) of the whole survey are then scaled to the well-defined standard stars. By applying this technique to the SDSS imaging data, 1 per cent internal accuracy has been achieved for $griz$ bands and about 2 per cent for u band by Padmanabhan et al. (2008).

More recently, Yuan et al. (2015; hereafter Y15) proposed a spectroscopy-based stellar color regression (SCR) method to provide accurate color calibrations for modern imaging surveys. As a test, this technique is applied to the SDSS Stripe 82 multi-epoch photometric data and achieved very high accuracies of ~ 5 mmag in $u-g$, ~ 3 mmag in $g-r$, and ~ 2 mmag

[1] South-Western Institute for Astronomy Research, Yunnan University, Kunming 650500, People's Republic of China; *yanghuang@ynu.edu.cn* (YH), *x.liu@ynu.edu.cn* (XWL)

[2] Department of Astronomy, Beijing Normal University, Beijing 100875, People's Republic of China; *yuanhb@bnu.edu.cn* (HBY)

[3] Department of Physics and Astronomy, Macquarie University, Sydney, NSW 2109, Australia

[4] School of Physics and Astronomy, Sun Yat-sen University, Zhuhai 519082, People's Republic of China

[5] Research School of Astronomy and Astrophysics, Australian National University, Canberra, ACT 2611, Australia

[6] Department of Physics, University of Notre Dame, Notre Dame, IN 46556, USA

[7] JINA Center for the Evolution of the Elements (JINA-CEE), East Lansing, MI 48823, USA

in $r-i$ and $i-z$. This method is very powerful and straightforward for calibrating modern large-scale photometric surveys, given the fact that most of the sky now covered by the massive spectroscopic surveys, e.g., the RAVE (Steinmetz et al. 2006), the SDSS/SEGUE (Yanny et al. 2009), the LAMOST (Deng et al. 2012; Liu et al. 2014) and the GALAH (De Silva et al. 2015) surveys. Moreover, with the uniform (photometric calibrations in the level of 2 mmag; Evans et al. 2018) all-sky three-bands photometry (G, $B_{\rm P}$, $R_{\rm P}$) released by Gaia DR2 (Gaia Collaboration et al. 2018), one can extend the SCR technique to calibrate individual photometric bands rather than the stellar colors (see Section 2 for more details).

The SMSS is an on-going digital image survey of the entire southern sky (Keller et al. 2007; Wolf et al. 2018). The survey depth is expected to 21-22 mag in all six optical bands ($uvgriz$). The SMSS is started in 2014 and includes two components: the shallow survey and the main survey. This short-exposure shallow survey reaches a depth of ~ 18 mag in all six bands, and the the collected images and resulted catalogues were published in SMSS DR1 (Wolf et al. 2018). The latest second data release has published portions of the main survey with detection limit down to > 21 mag in g and r filters (Onken et al. 2019; hereafter O19). In the SMSS DR2, the photometric zero points (ZPs) are anchored to the all-sky homogeneous Gaia DR2. O19 have first transformed the magnitudes of $B_{\rm P}$ and $R_{\rm P}$ of Gaia DR2 to the magnitudes of PS1 $griz$ using the relations provided by Tonry et al. (2018). Then the PS1 $griz$ are further converted to SkyMapper $ugriz$ using the transformations derived using synthetic photometry from the stellar spectral library of Pickles (1998). The internal tests by O19 show the reproducibility is 1 per cent in uv bands and 0.7 per cent in $griz$ bands. However, the bandpass transformations used in the calibrations could induce potential ZP systematics. First, they include dust correction terms in the transformations and the adopted values of extinction may suffer large errors (especially for the low Galactic latitude regions). This issue is more serious for uv bands since they are extrapolated from PS1 gi bands and the coefficients of the dust term are quite large (e.g., Casagrande et al. 2019). Secondly, the transformations do not consider the metallicity effects (very important for uv bands) and spatial patterns of the ZPs could be induced due to the stelar population gradients across the sky (also mentioned in O19).

In this paper, we re-calibrate the SMSS DR2 using the SCR method and aim to achieve a uniform photometry with accuracy better than 1 per cent. The paper is structured as follows. In Section 2, we briefly introduce the updated SCR technique with Gaia DR2 Photometry. The used data is described in Section 3. In Section 4, we perform the photometric re-calibration of SMSS DR2. Discussions and conclusion are finally presented in Section 5.

2. SCR WITH GAIA DR2 PHOTOMETRY

The idea of the SCR method is originated from the spectroscopic "star pair" technique (Yuan & Liu 2012; Yuan et al. 2013). The key steps and an example of its application to SDSS Stripe 82 photometric data of the SCR technique are presented in Y15. With the all-sky homogenous and accurate photometry achieved by Gaia DR2, we now can extend this technique to calibrate the photometric magnitudes of individual filters rather than the stellar colors only. A brief introduction of the extension of this method is given as follows. (1) Reference field with enough spectroscopic targets, located in the region with low extinction, and observed under good conditions is defined first. The relations between stellar intrinsic colors and atmospheric parameters (i.e., effective temperature $T_{\rm eff}$, surface gravity $\log g$ and metallicity [Fe/H] from spectroscopic surveys) are then determined. Here the intrinsic stellar color is a combination of the photometric band X to be calibrated and one of the Gaia photometric bands (G, $B_{\rm P}$, $R_{\rm P}$), after correcting for the interstellar reddening either from the extinction map of Schlegel et al. (1998; hereafter SFD) for high Galactic latitudes or the results estimated by the "star pair" technique (Yuan et al. 2013). In the Gaia era, $T_{\rm eff}$ in the relation could be replaced by $(B_{\rm P}-R_{\rm P})_0$, given their high photometric accuracies. (2) The X band magnitudes are predicted by the relation found in the former step using the atmospheric parameters, the Gaia photometry, and the interstellar reddening (given either by SFD map for high Galactic latitudes or "star pair" method). (3) The whole photometric data of the concerned survey are then internally calibrated to the selected reference filed by comparing the observed X band magnitudes to the predicted ones in color, magnitude, spatial and other spaces. (4) Finally, the internal calibrated photometric data can be further linked to the standard defined photometric system (e.g., AB or Vega) by well-defined standard stars observed in the survey.

3. DATA

In the current work, we calibrate the SMSS DR2 released last year (O19). The DR2 provide photometry in some filters (at either shallow or main survey depth) for the nearly entire southern Hemisphere (over 21 000 deg^2) and the data from the deep main survey in all six filters for over 7,000 deg^2 for the first time. In total, over 500 million unique sources and 5 billion individual detections from 120,000 images are contained in the released catalogues. As mentioned earlier, the internal reproducibility tests show a precision of 1 per cent in uv, and 0.7 per cent in $griz$, respectively.

To assist our SCR method to perform photometric calibrations of the SMSS DR2, the photometric data of Gaia DR2 (Gaia Collaboration et al. 2018) and the stellar atmospheric parameters ($T_{\rm eff}$, $\log g$, [Fe/H]) given by GALAH DR3 (Buder et al., to be submitted) are used in this work. Gaia DR2 has released three-bands (G, $B_{\rm P}$, $R_{\rm P}$) photometry for over 1.3 billion all-sky sources. The typical uncertainties of G and $B_{\rm P}$/$R_{\rm P}$ are 0.3 mmag and 2 mmag at $G \leq 13$ mag, 2 mmag and 10 mmag at $G = 17$ mag, and 10 mmag and 200 mmag at $G = 20$ mag, respectively (Gaia Collaboration et al. 2018). The ZPs of Gaia photometry are very stable across the whole sky with a precision of a few mmag (Evans et al. 2018). Stellar parameters ($T_{\rm eff}$, $\log g$, [Fe/H], $v_{\rm mic}$, $v_{\rm broad}$, $v_{\rm rad}$) and over 30 element abundances derived from $>$650 thousand spectra for over > 560 thousand unique stars are included in GALAH DR3. In the current work, only stellar atmospheric parameters of GALAH DR3 are used and the typical uncertainties are around 100 K, 0.15 dex and 0.10 dex for $T_{\rm eff}$, $\log g$ and [Fe/H], respectively, for FGK type stars with signal-to-noise ratio (SNR) greater than 20 per pixel. The footprints of GALAH DR3 now covered a large part (over 50 per cent, see Fig. 1) of the entire southern sky and it is very helpful to calibrate the large-scale photometric patterns of SMSS DR2.

We also use the $E(B-V)$ values from the SFD map. The values are corrected for a 14 per cent systematic overestimated in SFD map, as found in previous works (e.g., Schlafly et al. 2010; Yuan et al. 2013).

4. RECALIBRATION OF SMSS DR2

In this section, we recalibrate the current SMSS DR2 photometry (O19) using the upgraded SCR method described in Section 2.

4.1. *Reddening determinations and coefficients*

Given that the SMSS DR2 includes both low and high extinction regions, we apply the "star pair" method to GALAH DR3, together with Gaia DR2 photometry, to estimate the values of the color excesses and also derive the extinction coefficients of the Gaia passbands as a by products. To do so, we first define the control sample using the following criteria:

- GALAH spectral SNR greater than 20;
- $4000 \leq T_{\rm eff} \leq 7000\,{\rm K}$, $0 < \log g < 5$, and $-1.0 \leq {\rm [Fe/H]} \leq 5.0$;
- G, $B_{\rm P}$ and $R_{\rm P}$ photometry available from the Gaia DR2 and uncertainties smaller than 0.01 mag;
- $K_{\rm s}$ photometry available from the 2MASS and uncertainties smaller than 0.03 mag;
- Galactic latitudes $|b| \geq 30^{\circ}$ and SFD $E(B-V) \leq 0.02$ mag.

For the target sample, the SNR cut is loosed to 15 and the second to fourth criteria are the same as for the control sample. The last criterion is not used since we want to derive the extinction values for all GALAH targets. With above cuts, 459,239 and 19,201 stars are selected for the target and control sample, respectively.

Here, we derive the color excesses of $B_{\rm P}-R_{\rm P}$, $B_{\rm P}-G$, $E(G-R_{\rm P})$ and $E(G-K_{\rm s})$ for all the target stars using the "star pair" method described in Yuan et al. (2013, 2015) and Huang et al. (2019). First, the intrinsic colors of the control sample are derived by the SFD $E(B-V)$ values and an initial reddening coefficients from Chen et al. (2019) for Gaia passbands and Fitzpartrick (1999) for $K_{\rm s}$. Secondly, we estimate the intrinsic colors of each target star by assuming that the stellar intrinsic colors vary linearly with stellar atmospheric parameters ($T_{\rm eff}$, $\log g$, [Fe/H]) in a small box of the involved parameters[8], i.e., $|T_{\rm eff}^{\rm target,i} - T_{\rm eff}^{\rm control}| \leq 150\,{\rm K}$, $|\log g^{\rm target,i} - \log g^{\rm control}| < 0.25\,{\rm dex}$ and $|{\rm [Fe/H]}^{\rm target,i} - {\rm [Fe/H]}^{\rm control}| < 0.10\,{\rm dex}$. The color excesses are estimated by comparing the observed colors to the predicted intrinsic ones. Thirdly, the resulting color excesses are compared to SFD $E(B-V)$ at high latitudes ($|b| \geq 30^{\circ}$) to deliver empirical reddening coefficients (Fig. 1). Finally, we iterate the above steps until the resulting reddening coefficients converged to the one used to deredden the control sample.

The final resulted color excess ratios and extinction coefficients (by adopting $A_{K_{\rm s}} = 0.348$ from Fitzpartrick 1999) for Gaia passbands are presented in Table 1. Those coefficients found here are in great agreement with those derived by Chen et al. (2019). The values of color excess $E(B_{\rm P}-R_{\rm P})$ of over four hundred thousand GALAH target stars are converted to $E(B-V)$. By grouping the GALAH footprints into over 1000 fields of equal sky area (about 3.66 s.q. deg.), we compared the mean $E(B-V)$ of those fields estimated by the "star pair" technique to those from the SFD in the Galactic coordinate (see Fig. 2). The values of $E(B-V)$ from SFD map are in excellent agreement with those derived by the "star pair" method at high Galactic latitudes and low extinction regions, with a typical difference dispersion of 0.02 mag. However, one can clearly see that the SFD map overestimate the values of $E(B-V)$ at high extinction regions (typically at low Galactic latitudes) in Fig. 2. The using of SFD map in the passband transformations for photometric calibrations by SMSS DR2 will obviously contribute systematics to the ZPs for high extinction regions. The dereddened color and absolute magnitude diagram of the GALAH targeted stars is shown in Fig. 3. Here, the distances estimated by Bailer-Jones

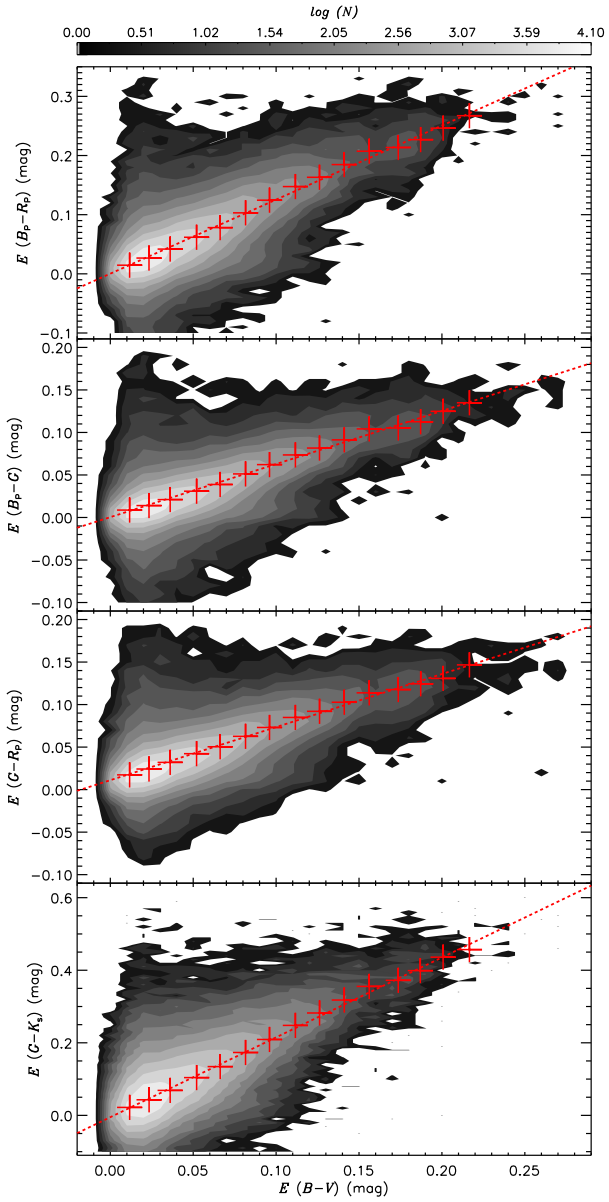

Figure 1. Color excesses $B_{\rm P}-R_{\rm P}$, $B_{\rm P}-G$, $G-R_{\rm P}$ and $G-K_{\rm s}$ versus SFD $E(B-V)$. In each pannel, the color-coded contour of the stellar number density in logarithmic scale is shown. Red plus signs denote median values obtained by binning the data points into 15 groups with a bin size of 0.015 mag in $E(B-V)$. The median values in the individual bins are calculated with a 3σ clipping procedure. The bred dashed lines are first-order polynomial fits to the red plus signs, where each point carries equal weight.

[8] We require at least 20 stars from the control sample to derive the intrinsic colors of each target star.

Table 1
Color excess ratios and extinction coefficients for Gaia passbands

$\frac{E(B_P-R_P)}{E(B-V)}$	$\frac{E(B_P-G)}{E(B-V)}$	$\frac{E(G-R_P)}{E(B-V)}$	$\frac{E(G-K_s)}{E(B-V)}$	R_G	R_{B_P}	R_{R_P}
1.252 ± 0.026	0.625 ± 0.012	0.624 ± 0.012	2.200 ± 0.035	2.548 ± 0.035	3.173 ± 0.037	1.924 ± 0.037

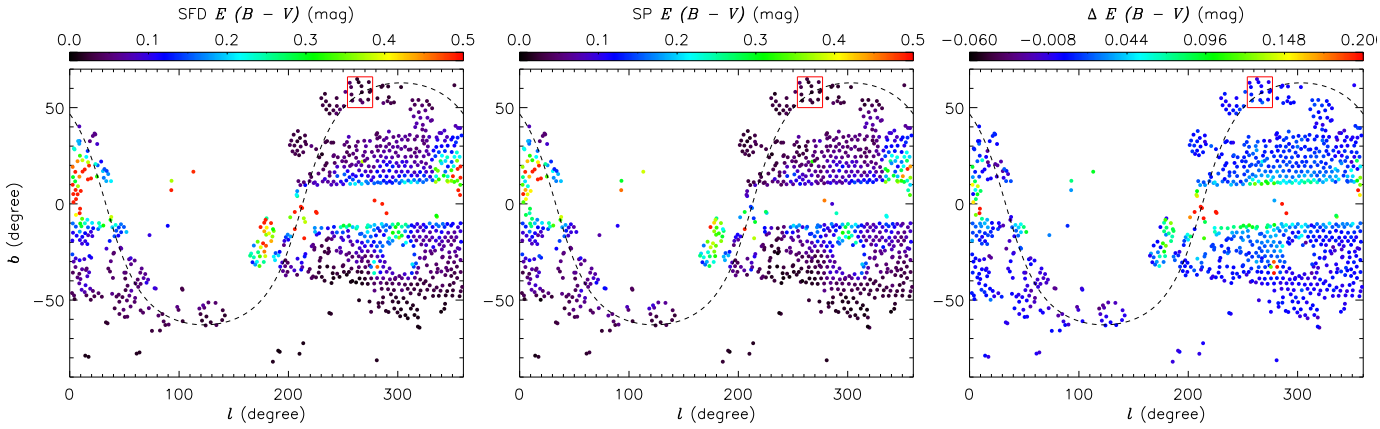

Figure 2. $E(B-V)$ distribution from the SFD map (left panel) and "star pair" method (middle panel; see Section 4.1) for GALAH DR3 footprints. The right panel shows the difference of $E(B-V)$ between SFD map and "star pair" estimates. Each dot here represents a sub-field of about 3.66 s.q. deg. divided from over four hundred thousand GALAH targets (see Section 4.1 for details) by the HEALPix (Gorski et al. 2005). The color of each dot shows the mean value of $E(B-V)$ or $E(B-V)$ difference. The red box marked in each panel represents the reference field for SMSS DR2 photometric calibration (see Section 4.2).

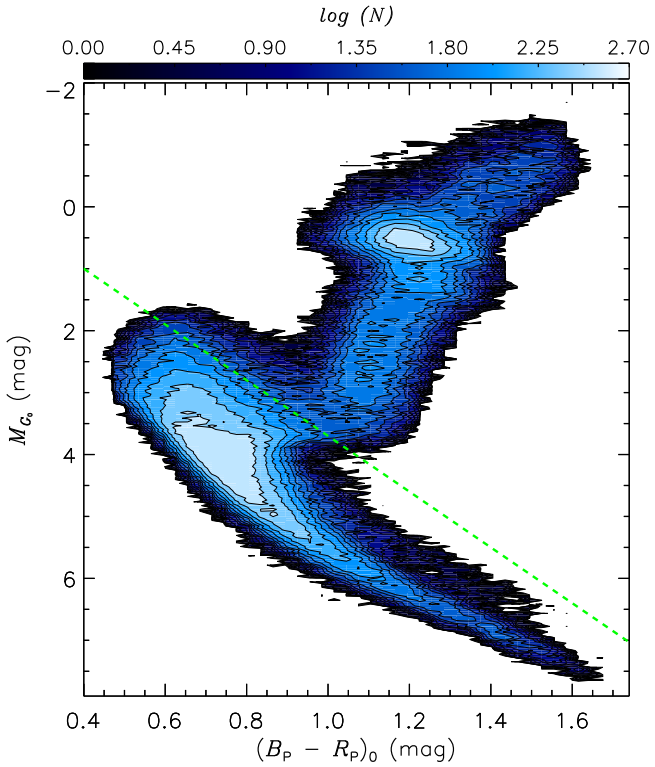

Figure 3. Dereddened color and absolute magnitude diagram of stars with color excess $E_{B_P-R_P}$ estimated by "star pair" method (see Section 4.1). The logarithmic color scale represents the stellar number density. The dashed line represents an empirical cut, i.e., $M_{G_0} = -0.8 + 4.5(B_P - R_P)_0$, to separate dwarf and giant stars.

et al. (2018) using the Gaia DR2 parallaxes are used to derive the absolute magnitudes M_{G_0} (by requiring parallax relative errors smaller than 30 per cent).

If note specified, the color excesses $E(B_P - R_P)$ estimated by "star pair are adopted in the following reddening corrections. For the extinction coefficients, we adopt the values in Table 1 for Gaia passbands and the values in Table 7 of Huang et al. (2019) for SkyMapper passbands.

4.2. *Predictions of SkyMapper magnitudes*

In this section, the SkyMapper magnitudes of $uvgriz$ bands are predicted using the SCR technique. We only use dwarf stars and thus the effects of surface gravity $\log g$ (roughly around 4.0 dex) on the stellar intrinsic colors can be neglected. The dwarf stars are selected by using an empirical cut on the $(B_P - R_P)_0 - M_{G_0}$ plane (see Fig. 2). In total, 234,413 dwarf stars with $E(B_P - R_P)$ estimates, Gaia DR2 photometry, SMSS photometry and GALAH DR3 atmospheric parameters are selected. As mentioned in Section 3, we need define a reference filed with enough GALAH targets. In addition, this field should better locate at low extinction region and thus the SMSS DR2 photometric calibrations are not affected by the dust terms. To do so, region of $254^\circ \leq l \leq 277^\circ$ and $50^\circ \leq b \leq 66^\circ$ is defined as the reference field. The dwarf stars of this reference field satisfying the following criteria are then used to build the metallicity-dependent intrinsic color-color relations:

- SFD $E(B-V) \leq 0.03$ mag;
- good photometry quality from the SMSS DR2: *x_good* ≥ 1, *x_flags* ≤ 3, *e_x_psf* ≤ 0.05 mag, *class_star* ≥ 0.9, here x represents $u/v/g/r/i/z$ band;
- $g \geq 12$ mag, $r \geq 11.8$ mag and $i \geq 11.0$ mag to avoid saturation;

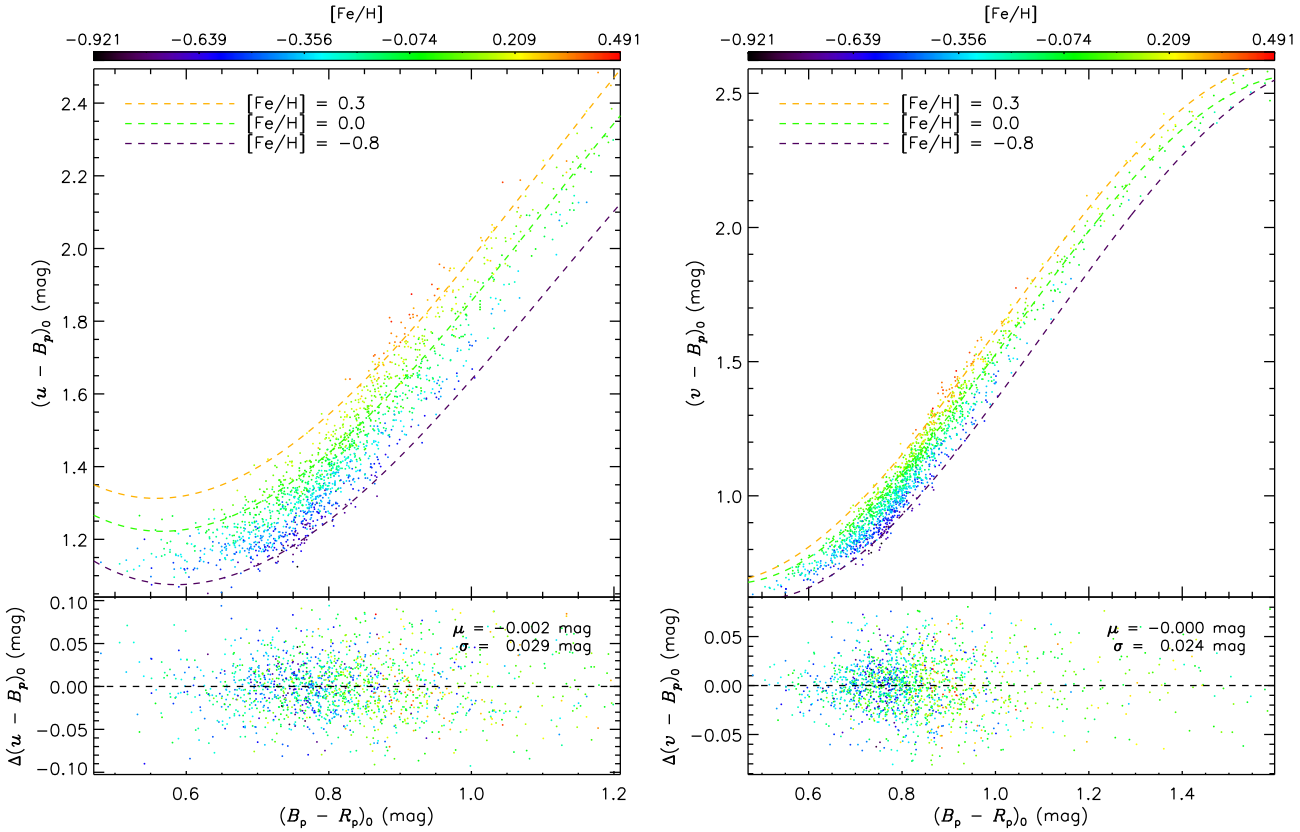

Figure 4. Metallicity-dependent intrinsic color-color relation for $(u - B_{\rm P})_0$ (left panel) and $(v - B_{\rm P})_0$ (right panel) versus $(B_{\rm P} - R_{\rm P})_0$. The colors of data points represent their metallicity as indicated by the top color bar. The dashed lines represent our best fits for selected values of [Fe/H] as marked in the top-left corner of each panel. The bottom plot in each panel shows the fit residual with the median and standard deviation values marked in the top-right corner.

- good photometry quality from the Gaia DR2: the photometric uncertainties in G, $B_{\rm P}$ and $R_{\rm P}$ bands are all smaller than 0.01 mag.

In total, over 1500 GALAH targeted dwarf stars are selected in the reference field. Using those dwarf stars, we have performed third-order 2D polynomial (with 10 free parameters) fitting to their dereddened $u - B_{\rm P}$, $v - B_{\rm P}$, $g - B_{\rm P}$, $r - G$, $i - R_{\rm P}$ and $R_{\rm P} - z$ colors as a function of $(B_{\rm P} - R_{\rm P})_0$ and [Fe/H]. The scatter of the fit residuals are 0.029, 0.024, 0.008, 0.008, 0.005 and 0.007 mag for colors $u - B_{\rm P}$, $v - B_{\rm P}$, $g - B_{\rm P}$, $r - G$, $i - R_{\rm P}$ and $R_{\rm P} - z$, respectively. As an example, the fitting results of colors $u - B_{\rm P}$ and $v - B_{\rm P}$ are shown in Fig. 4.

We apply the above metallicity-dependent intrinsic color-color relations to all the dwarfs selected above to predict SkyMapper $uvgirz$ magnitudes, using Gaia photometry, GALAH [Fe/H] and $E(B_{\rm P} - R_{\rm P})$ color excesses. Here, we require those dwarfs to satisfy the second to forth criteria for stars of the reference field. In total, SkyMapper $uvgirz$ magnitudes of over 210,000 dwarf stars are predicted in this way. As Fig. 5 plots, the predicted SkyMapper magnitudes are compared to the observed ones from SMSS DR2. Generally, significant ZP systematics are detected for uv bands when compared the observed magnitudes to the predicted ones. For $griz$ bands, the observed magnitudes agrees with the predicted ones within 10 mmag.

4.3. *Dependence on reddening*

As mentioned earlier, the ZPs of SkyMapper photometry could show dependences on the extinction values due to the dust terms including in the passband transformations for constructing photometry calibrators from the Gaia DR2. We therefore first check the differences between the predicted magnitudes and the observed magnitudes as a function of SFD $E(B - V)$. The results are listed in Table A1 and shown in Fig. 5. As expected, the median differences are nearly zero at SFD $E(B - V) \leq 0.04$ mag and then gradually increase with SFD $E(B - V)$. The systematics can reach as large as 0.24, 0.23, 0.03, 0.02, 0.04 and 0.05 mag for $uvgriz$, respectively at SFD $E(B - V) \sim 0.50$ mag. For large SFD $E(B - V)$ range (> 0.3 mag), the ZP systematics tend to be stable or slightly declining. This is because O19 adopted extinction values from SFD map for $E(B - V) < 0.3$ mag, and from the combination of SFD map and the Gaia estimates of A_G (Andrae et al. 2018) for $E(B - V) \geq 0.3$ mag in the passband transformations. The partly use of A_G estimates from Gaia for high extinction region could relieve the overestimates of the dust terms by SFD map and thus the ZP systematics tend to be flat/declining at high $E(B - V)$ range. But the uncertainties of Gaia A_G estimates are quite large, caused large scatters of the magnitude differences at high extinction range.

Again as expected, the reddening dependent ZP systematics are very large for uv bands since they are extrapolated from optical bands and the coefficients of the dust term in the passband transformations are quite large (ten to hundred times larger than those for other bands). The ZP of r band shows the

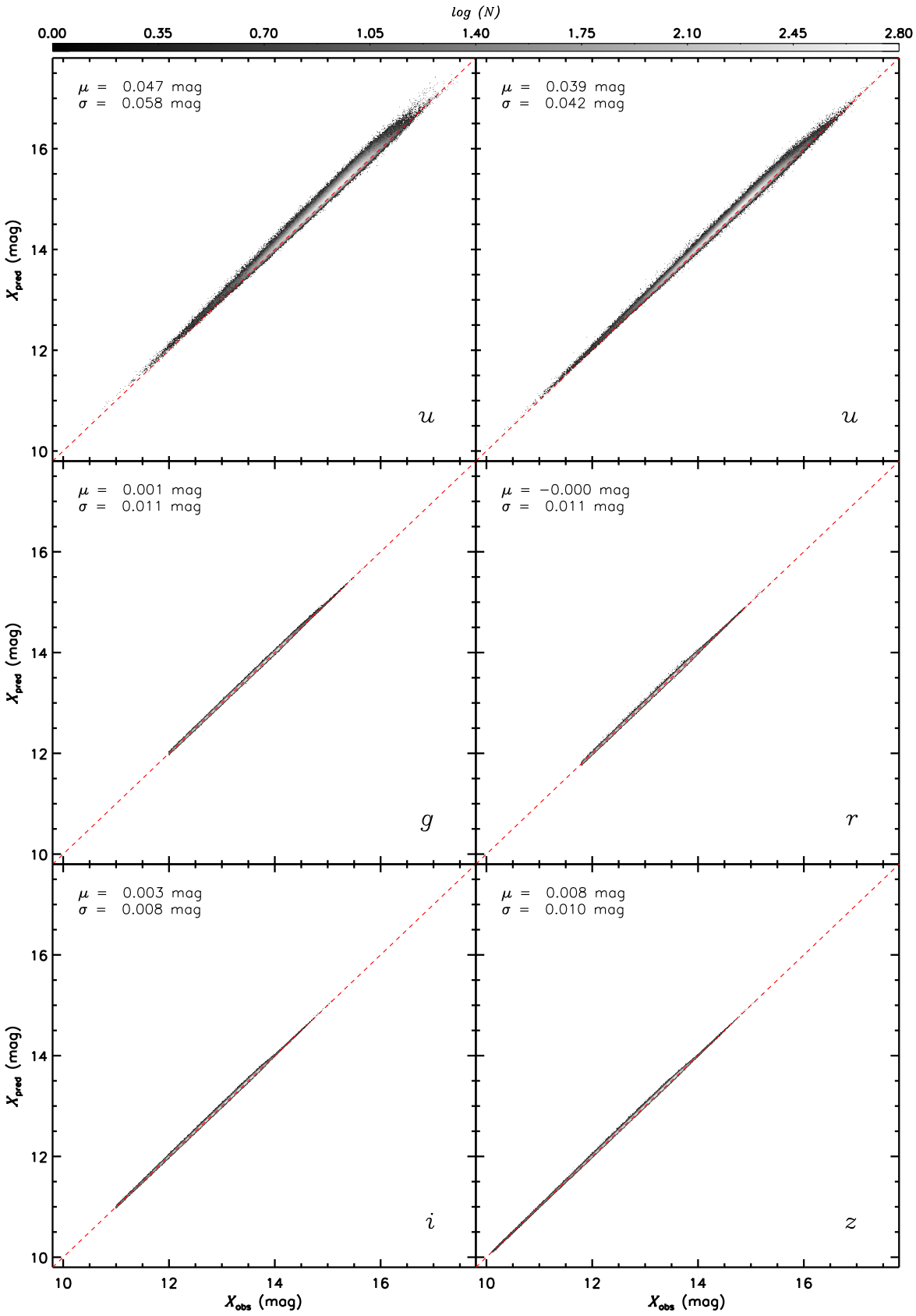

Figure 5. Comparisons of the predicted SkyMapper magnitudes with those observed ones from SMSS DR2. In each panel, the color-coded contour of the stellar number density in logarithmic scale is shown. The values of the median and standard deviations of the differences between the predicted and observed magnitudes are marked in the top-left corner of each panel.

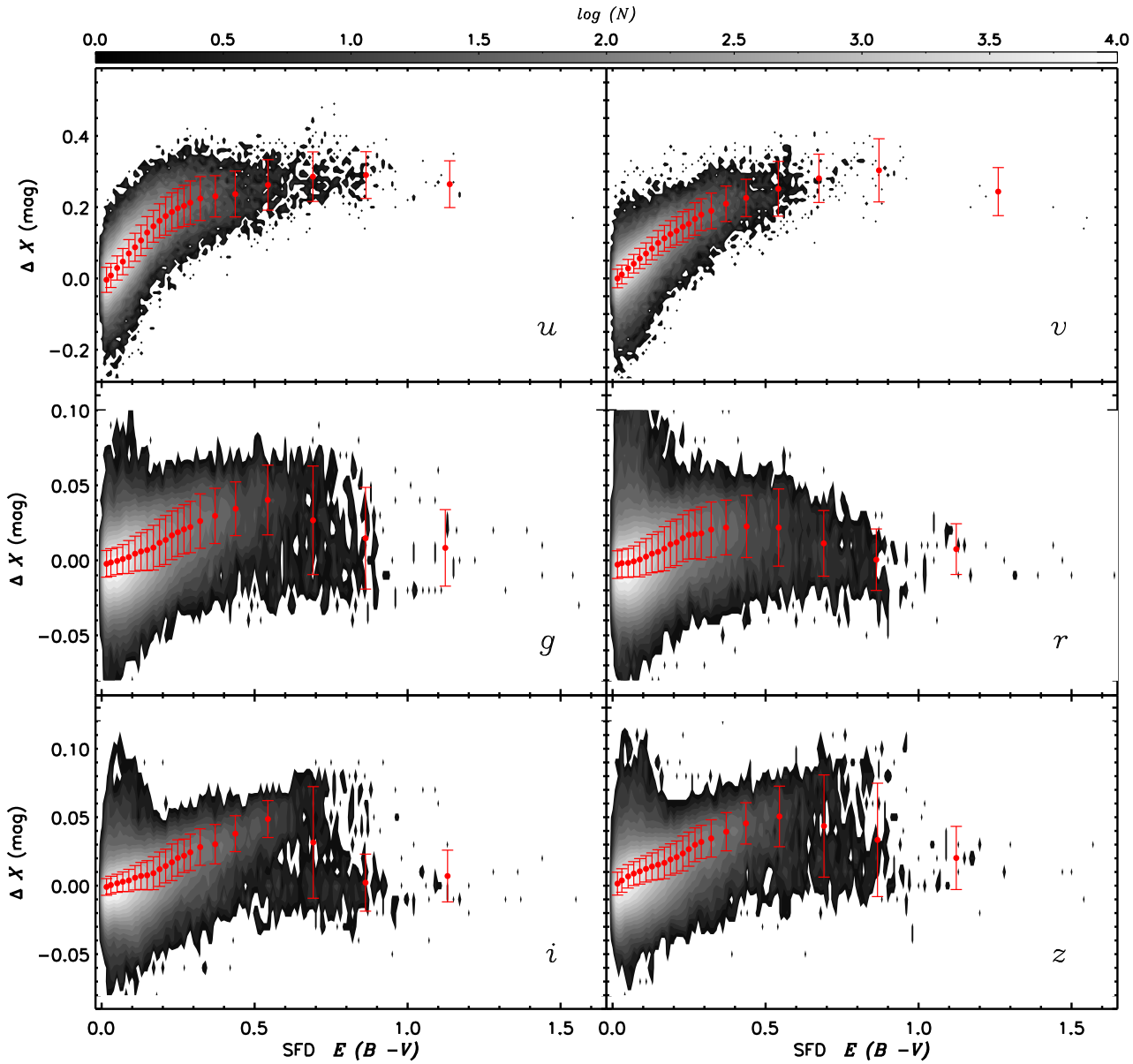

Figure 6. Magnitude offsets (predicted one minus observed one) as a function SFD $E(B-V)$ for $uvgriz$. The red dots in each panel represent the median values of each SFD $E(B-V)$ bin and the bin ranges are given in Table A1. The error bars indicate the standard deviations of the magnitude differences of each SFD $E(B-V)$ bin. The logarithmic color scale represents the stellar number density.

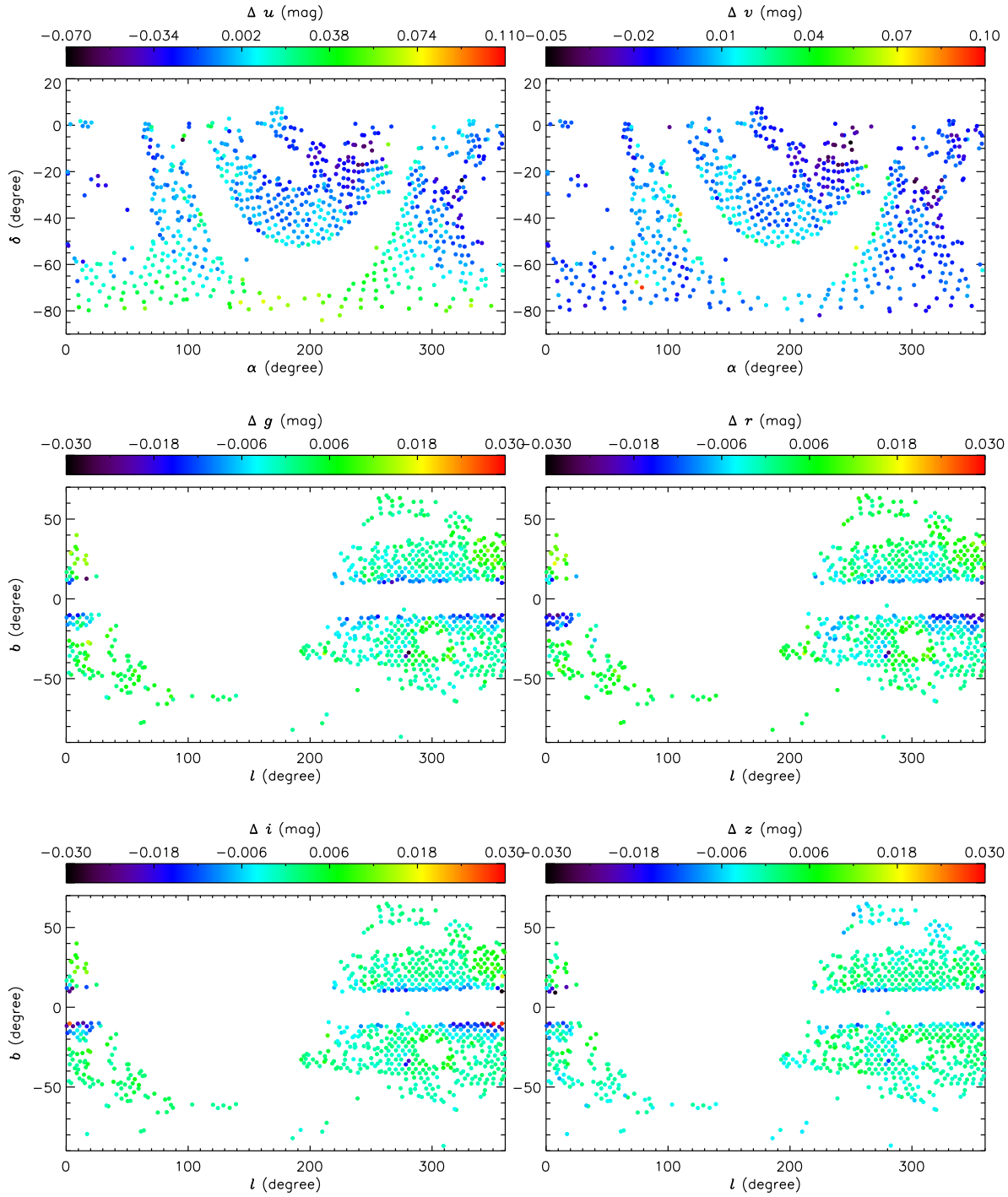

Figure 7. Distributions of the median magnitude differences (predicted minus observed that corrected for the reddening dependent systematics) in equatorial coordinate system for uv bands (the top two panels) and in Galactic coordinate system for $griz$ bands (the bottom four panels). Each dot here represents a field of about 3.66 s.q. deg. divided by the HEALPix (Gorski et al. 2005). The color of each dot shows the median value of magnitude differences of specified bands.

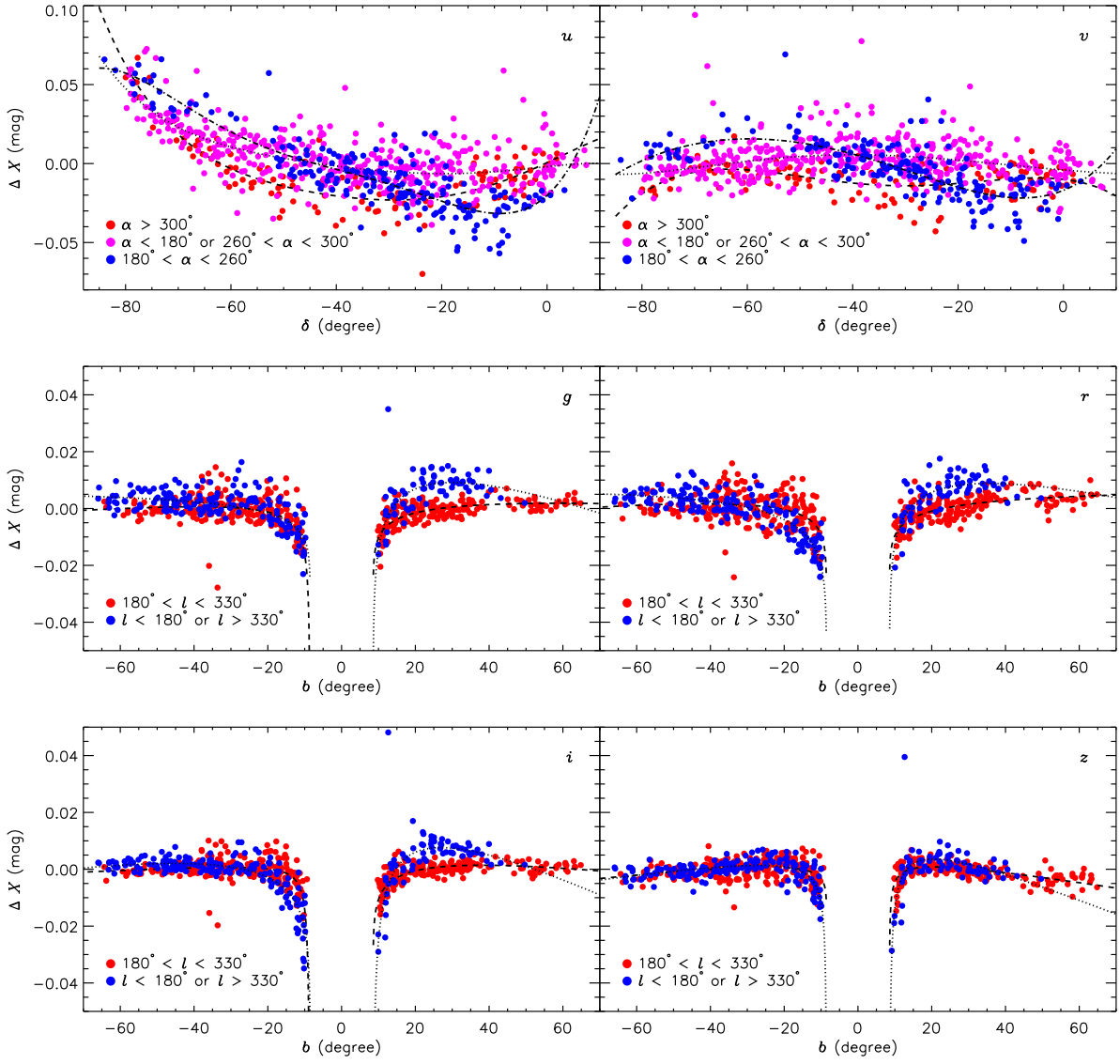

Figure 8. The median magnitude differences (same as those dots in Fig. 7) as a function of Declination (δ) for different Right Ascension (α) bins (uv bands, the top two panels) or Galactic latitude (b) for different Galactic longitude (l) bins ($griz$ bands, the bottom four panels). The different colors indicate data points of different α or l ranges. The different types of line represent the best-fits described in Section 4.4.

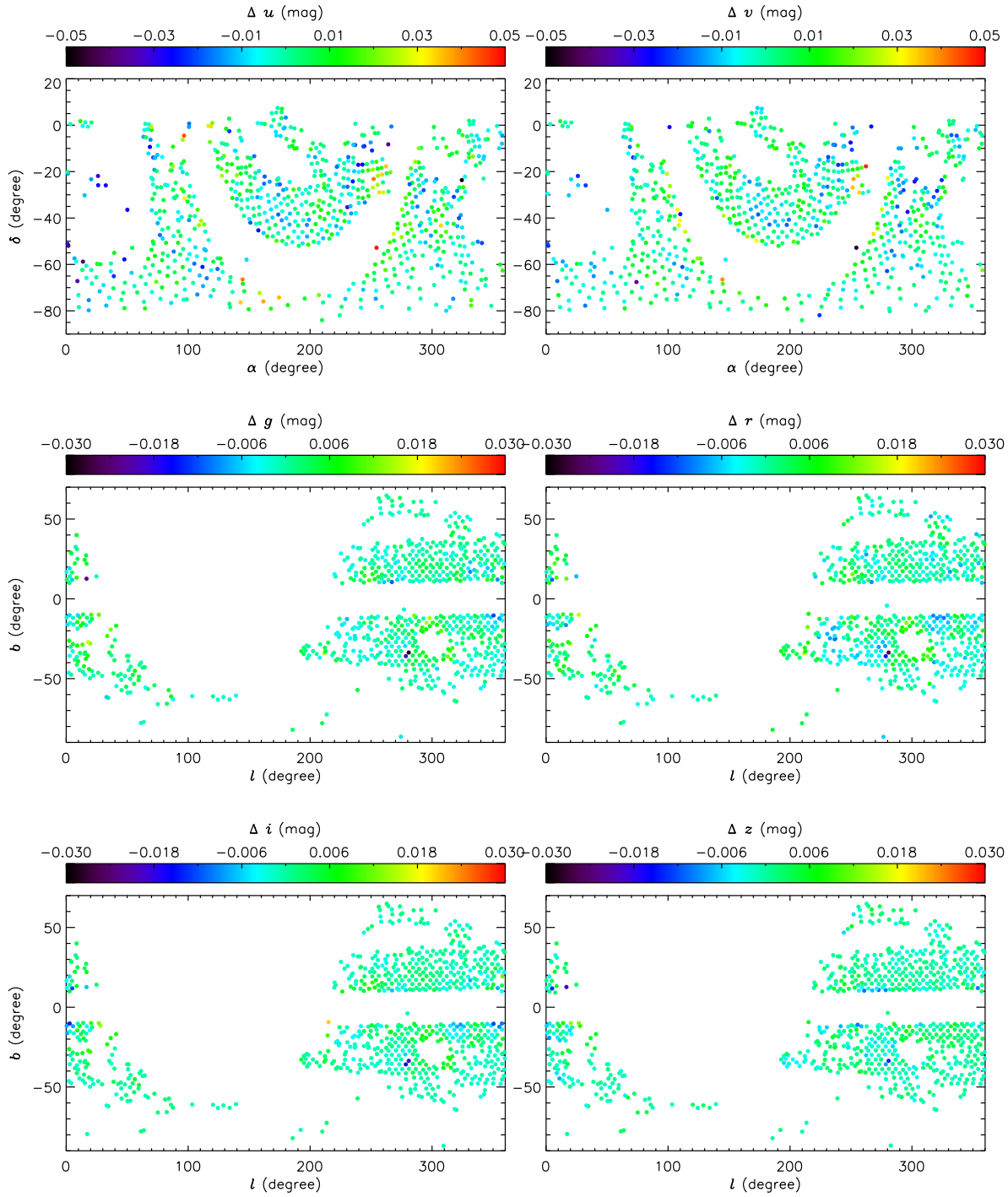

Figure 9. Same as the Fig. 7 but the observed magnitudes have been corrected for both reddening dependent and spatial systematics.

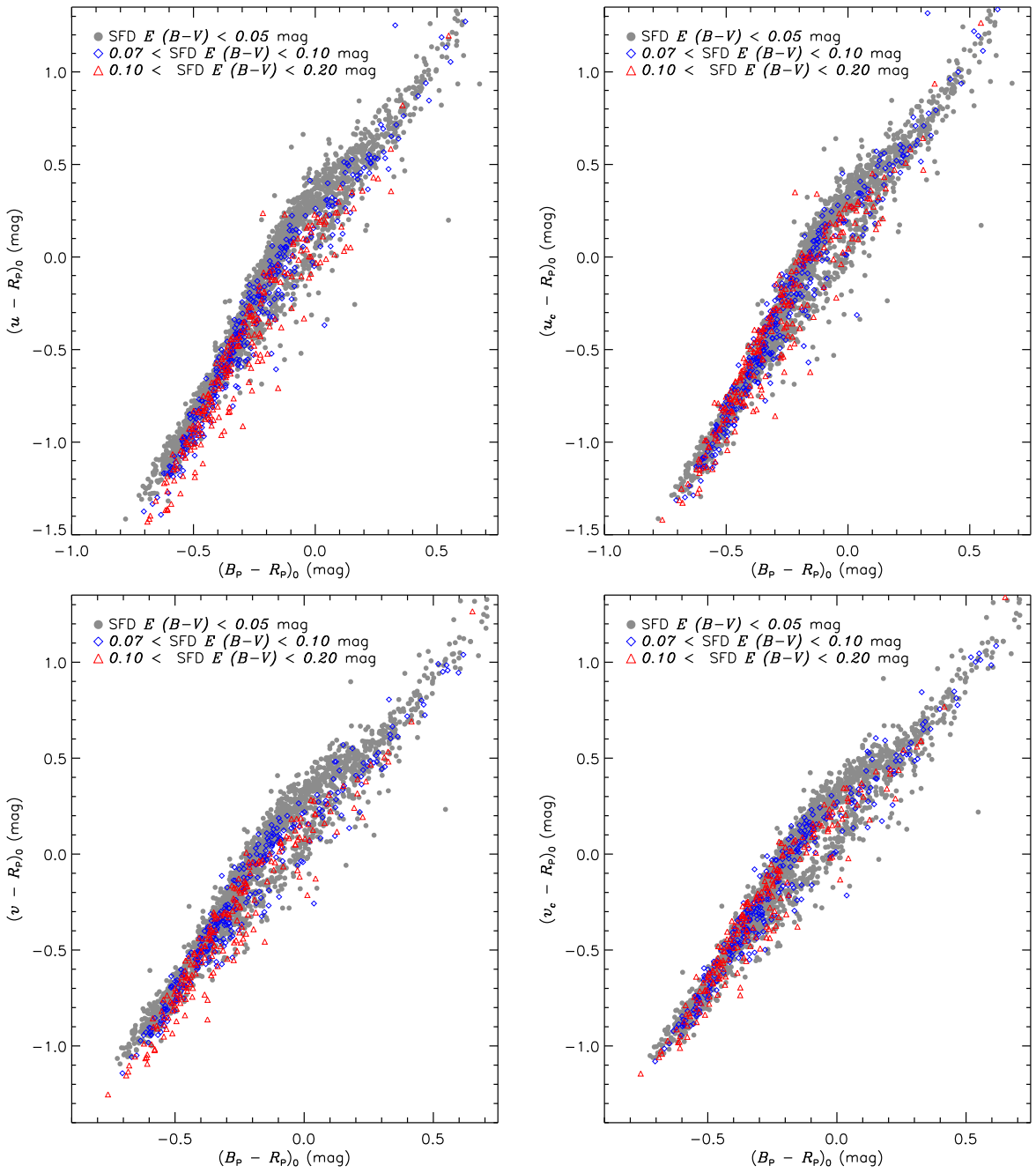

Figure 10. Stellar locus $(u/v - R_{\rm P})_0$ versus $(B_{\rm P} - R_{\rm P})_0$ of WDs. The top two panels show the locus at u band with the left one from the SMSS DR2 and the right one from the re-calibrated photometry. The bottom two panels are the same as the above but for v band. Grey dots, blue diamonds and red triangles represent WDs with SFD $E(B-V)$ of < 0.05 mag, between 0.07 and 0.10 mag, and between 0.10 and 0.20 mag, respectively.

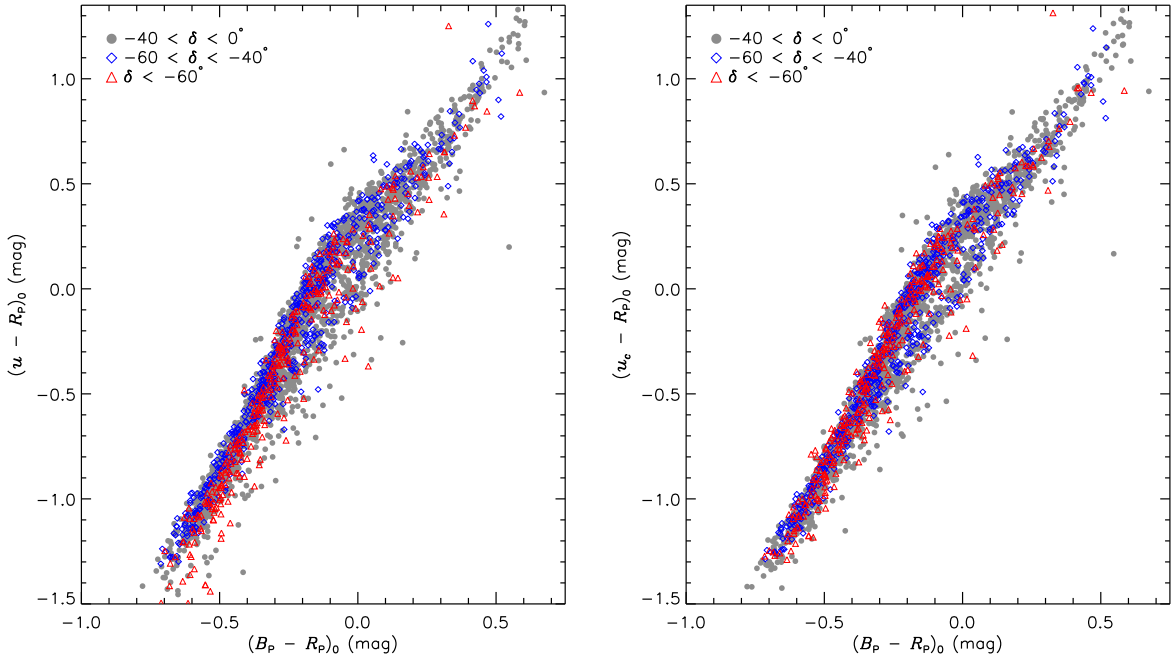

Figure 11. The WD locus $(u - R_{\rm P})_0$ versus $(B_{\rm P} - R_{\rm P})_0$ of different δ bins, with the left panel from the SMSS DR2 and the right one from the re-calibrated photometry. Grey dots, blue diamonds and red triangles represent WDs located at $-40 < \delta < 0°$, $-60 < \delta < -40°$ and $\delta > -60°$, respectively.

smallest variations with SFD $E(B-V)$ due to its smallest coefficients of the dust term in the transformation. In this sense, we believe that the reddening dependent ZP systematics of the SkyMapper photometry are largely from the dust terms in the passband transformations (for the photometric calibration purpose).

4.4. *Spatial variations*

After correcting for the reddening dependent ZP systematics using the values listed in Table A1, we further check the spatial variations of ZPs of SMSS DR2. To do so, we divide the above >200,000 dwarfs into over 700 fields of equal sky area (about 3.66 s.q. deg.) with at least 50 stars in each field[9]. The median values of the magnitude differences (predicted minus observed) of each field are calculated and shown in Fig. 8. The ZPs of all the six bands show significant spatial variations. For uv bands, the ZPs are mainly varied with Declination (δ) but show different behaviors for different Right Ascension (α) bins. The ZP spatial patterns along δ of the uv bands are possibly from the residuals of the corrections of atmospheric extinction (especially in the u band). Clear positive ZPs are seen around the Southern Celestial Pole ($\delta < -70°$; thus large values of airmass and atmospheric extinction) in u band. To remove the spatial patterns of ZPs, we have performed fifth- and fourth-order polynomials fitting to the u and v band ZP systematics as a function of δ for different α ranges, respectively. The fitting results and coefficients are presented in Fig. 8 and Table A2, respectively.

For $griz$ bands, the ZPs are close to zero at high Galactic latitude (b) regions and rapidly decrease with b at low latitude regions. To correct this b dependent systematics, we fit the ZPs as a function of b for $griz$ bands with the equations as follows:

$$\Delta X = a_0 + a_1(|b| - 8.5)^{a_2} + a_3 b, \qquad (1)$$

here X represents the concerned band (i.e., $griz$). The fitting results and coefficients are again presented in Fig. 8 and Table A2, respectively.

We also check the ZPs of SMSS DR2 in other spaces, e.g., magnitude, color, and no significant variations are detected.

4.5. *Final accuracies*

After properly correcting for the reddening dependent and spatial systematics, the final median magnitude differences of the over 700 fields are shown in Fig. 9. As the plot shows, the ZPs of most of the re-calibrated regions are with 10 mmag. Detailedly, the ZPs of 50 per cent fields are within 6.7, 5.7, 2.1, 2.5, 1.5 and 1.6 mmag for $uvgriz$, respectively. For 90 per cent fields, the ZPs are better than 18.5, 17.0, 5.7, 6.9, 5.0, 4.7 mmag for $uvgriz$, respectively. The accuracies of the ZPs of the SMSS DR2 photometry could be further improved (see more discussions in Section 5.1).

4.6. *External checks with the white dwarf locus*

All the above photometric systematics found for the SMSS DR2 are relied on the SCR method. Here, we provide an independent check of the re-calibration by the SCR, using the white dwarf (WD) locus. The locus should be very stable and uniform for WDs at different spatial locations and with different values of the reddening.

We first cross match the white dwarf catalog constructed by Gentile Fusillo et al. (2019) from the Gaia DR2 to the SMSS DR2. We require the WDs with Galactic latitude higher than 20°, allowing one to correct the reddening using SFD map. In addition, the WD probability ($P_{\rm WD}$) is required to be higher than 0.75 and the uncertainties of Gaia $B_{\rm P}$ and $R_{\rm P}$ are smaller than 0.015 mag. Here, we only check the uv bands since the photometric systematics in other four bands are relatively

[9] This number of star can allow us to perform photometric calibration in few mmag level for individual fields, given the predicted accuracies of magnitudes for individual stars (see Fig. 4 and Section 4.2).

small and hard to be examined by the WD locus. The photometric uncertainties of uv bands are required to be smaller than 0.05 mag. In total, over 3000 and 4000 WDs with good photometric qualities in u and v band are left.

The stellar locus, $(u/v-R_{\rm P})_0$ versus $(B_{\rm P}-R_{\rm P})_0$, of those WDs are shown in Fig. 10. Here, the reddening corrections are done with the SFD map. As the plot shows, the WD locus given by the SMSS DR2 with SFD $E(B-V) > 0.07$ mag deviate the one with SFD $E(B-V) < 0.05$ mag significantly, for both u and v bands. The deviations are roughly consistent with the values presented in Table A1. The WD loci of different SFD $E(B-V)$ bins given by our re-calibrated photometry are consistent with each other very well, implying the power of our SCR method in calibrating the photometric ZPs.

Finally, we also show the WD loci of different δ bins at u band in Fig. 11. Again, the locus derived by the SMSS DR2 show significant deviations for different δ bins while those loci derived by our re-calibrated photometry agree with each other.

5. DISCUSSIONS AND CONCLUSION

5.1. *Caveats of the current calibration*

With the SCR technique, Gaia DR2 photometry and GALAH stellar parameters, we have re-calibrated the SMSS DR2 photometry and achieve a ZP accuracy of < 1 per cent for most of the fields. However, there are several caveats of the current calibrations.

First, the current calibrations are only performed for the GALAH footprints not the full sky coverages of the SMSS DR2. Some unknown photometric systematics could present in the regions not covered by the GALAH DR3 and thus still remain in the re-calibrated photometry. To solve this problem, we could further implement the "ubercalibration" to try achieve a homogenous internal calibration for the whole SMSS sky coverage by using the overlapping regions. In addition, the future GALAH observations could help calibrate more missing regions.

Secondly, the current SCR method assumes constant reddening coefficients of the Gaia and SkyMapper passbands for different positions and spectral energy distributions (SEDs) of stars. As we know, the extinction law could change with different environments (spatial locations) and also the coefficients are dependent on the stellar SED (especially for the Gaia broad bands). The current assumptions of the reddening coefficients obviously could contribute some systematics in the re-calibrations. However, this error should be minor compared to the existing systematics in the SMSS DR2. First, most of the calibrated fields belong to normal diffuse environment and they should follow a universal extinction law with a small scatter (e.g., Schlafly et al. 2010; Yuan et al. 2013). In addition, most of the dwarfs we adopted to do calibration are F/G-type stars with a quite narrow color in $(B_{\rm P}-R_{\rm P})_0$ (mainly between 0.60 and 0.8 mag; see Fig. 3). The extinction coefficient variations due to the various stellar SEDs are therefore quite small. As a next step, the two effects should be properly considered to further improve the photometric ZP accuracy of the SMSS.

Finally, we do not anchor the scale of the re-calibrated photometry to the well-defined AB or Vega photometric systems. As mentioned earlier, this could be done by comparing the re-calibrated photometry to a few well-defined photometric standard stars. However, there no well-defined photometric standard stars for the SkyMapper filter systems. Another method is to integrate synthetic SkyMapper magnitudes on AB/Vega photometric systems by using the spectro-photometric standard stars from the Next Generation Spectral Library[10] and the CALSPEC spectral library (Bohlin, Gordon & Tremblay 2014). But most of those stars are too bright and saturate in the SMSS DR2. We encourage the SkyMapper team to observe few of those standard stars with very short exposure to avoid saturation in the future.

5.2. *Conclusion and SCR+Gaia perspective for future large-scale photometric surveys*

We have applied the SCR technique, together with the Gaia DR2 photometry and the GALAH DR3 atmospheric parameters, to re-calibrate the ZPs of the SMSS DR2. As we expected, strong reddening dependent ZP systematics are detected for all six SkyMapper bands ($uvgriz$). The photometric ZPs first tend to zero at low extinction regions and then gradually increase with SFD $E(B-V)$, and can reach as large as 0.24, 0.23, 0.03, 0.02, 0.04 and 0.05 mag for $uvgriz$, respectively at high extinction regions with SFD $E(B-V) \sim 0.50$ mag. This reddening dependent trend of the photometric ZPs is largely caused by the dust terms in the passband transformations for constructing the photometric calibrators. Our study also shows small but significant spatial variations of the ZPs. Finally, by properly correcting for the reddening dependent and spatial ZP systematics, most of the calibrated fields have ZP uncertainties smaller than 10 mmag. The independent checks by WD locus also show the power of our SCR method in calibrating the SMSS DR2 photometry.

In the current work, we show that the power of the SCR method in calibrating the modern digital photometric surveys to < 1 per cent accuracy . The bases of this technique are massive large-scale spectroscopic surveys and an independent all-sky uniform photometric survey. The latter now is easy to achieve since we have the Gaia DR2 and are promised with better all-sky photometry in the future releases of the Gaia. The former now is also not a problem. In the northern sky, we have the LAMOST spectroscopic surveys achieved over ten million spectra covering most of the northern sky ($-10 < \delta < 60^\circ$). In the southern sky, we have the GALAH spectroscopic surveys and the 4MOST (de Jong et al. 2019) in the near future. The only problem of the current massive spectroscopic surveys is the bright limiting magnitude (compared to the photometric surveys). We therefore encourage the ongoing/planning surveys to have short exposure shallow surveys first. After calibrating those shallow surveys with our SCR technique, they are the second-level photometric standards for the faint main surveys. To conclude, we believe the SCR would be a promising method to calibrate lots of ongoing/planning large-scale digital sky surveys (e.g., the LSST, the Mephisto and the J-PAS) to achieve photometric ZPs in few mmag level.

ACKNOWLEDGEMENTS

The Guoshoujing Telescope (the Large Sky Area Multi-Object Fiber Spectroscopic Telescope, LAMOST) is a National Major Scientific Project built by the Chinese Academy of Sciences. Funding for the project has been provided by the National Development and Reform Commission. LAMOST is operated and managed by the National Astronomical Observatories, Chinese Academy of Sciences.

[10] https://archive.stsci.edu/prepds/stisngsl/

This work is supported by National Natural Science Foundation of China grants 11903027, 11973001, 11833006, 11811530289, U1731108, and U1531244, and National Key R&D Program of China No. 2019YFA0405503. Y.H. is supported by the Yunnan University grant C176220100007.

The national facility capability for SkyMapper has been funded through ARC LIEF grant LE130100104 from the Australian Research Council, awarded to the University of Sydney, the Australian National University, Swinburne University of Technology, the University of Queensland, the University of Western Australia, the University of Melbourne, Curtin University of Technology, Monash University and the Australian Astronomical Observatory. SkyMapper is owned and operated by The Australian National University's Research School of Astronomy and Astrophysics. The survey data were processed and provided by the SkyMapper Team at ANU. The SkyMapper node of the All-Sky Virtual Observatory (ASVO) is hosted at the National Computational Infrastructure (NCI). Development and support the SkyMapper node of the ASVO has been funded in part by Astronomy Australia Limited (AAL) and the Australian Government through the Commonwealth's Education Investment Fund (EIF) and National Collaborative Research Infrastructure Strategy (NCRIS), particularly the National eResearch Collaboration Tools and Resources (NeCTAR) and the Australian National Data Service Projects (ANDS).

This work has made use of data from the European Space Agency (ESA) mission *Gaia* (https://www.cosmos.esa.int/gaia), processed by the *Gaia* Data Processing and Analysis Consortium (DPAC, https://www.cosmos.esa.int/web/gaia/dpac/consortium). Funding for the DPAC has been provided by national institutions, in particular the institutions participating in the *Gaia* Multilateral Agreement.

APPENDIX

A. TABLES FOR CORRECTING THE REDDENING DEPENDENT AND SPATIAL ZP ERRORS OF SMSS DR2 PHOTOMETRY

Table A1 lists the magnitude offsets as a function of SFD $E(B-V)$. Table A2 lists the fit coefficients for the magnitude offsets as a function of δ and b for uv and $griz$, respectively.

REFERENCES

Abbott, T. M. C., Abdalla, F. B., Avila, S., et al. 2019, Phys. Rev. D, 99, 123505
Andrae, R., Fouesneau, M., Creevey, O., et al. 2018, A&A, 616, A8
Bailer-Jones, C. A. L., Rybizki, J., Fouesneau, M., Mantelet, G., & Andrae, R. 2018, AJ, 156, 58
Benitez, N., Dupke, R., Moles, M., et al. 2014, arXiv e-prints, arXiv:1403.5237
Bohlin, R. C., Gordon, K. D., & Tremblay, P.-E. 2014, PASP, 126, 711
Casagrande, L., Wolf, C., Mackey, A. D., et al. 2019, MNRAS, 482, 2770
Chambers, K. C., Magnier, E. A., Metcalfe, N., et al. 2016, arXiv:1612.05560
Chen, B.-Q., Huang, Y., Yuan, H.-B., et al. 2019, MNRAS, 483, 4277
Dark Energy Survey Collaboration, Abbott, T., Abdalla, F. B., et al. 2016, MNRAS, 460, 1270
Deng, L.-C., Newberg, H. J., Liu, C., et al. 2012, Research in Astronomy and Astrophysics, 12, 735
de Jong, R. S., Agertz, O., Berbel, A. A., et al. 2019, The Messenger, 175, 3
Evans, D. W., Riello, M., De Angeli, F., et al. 2018, A&A, 616, A4
Finkbeiner, D. P., Schlafly, E. F., Schlegel, D. J., et al. 2016, ApJ, 822, 66
Fitzpatrick, E. L. 1999, PASP, 111, 63
Gaia Collaboration, Brown, A. G. A., Vallenari, A., et al. 2016, A&A, 595, A2
Gaia Collaboration, Brown, A. G. A., Vallenari, A., et al. 2018, A&A, 616, A1
Gentile Fusillo, N. P., Tremblay, P.-E., Gänsicke, B. T., et al. 2019, MNRAS, 482, 4570
Górski, K. M., Hivon, E., Banday, A. J., et al. 2005, ApJ, 622, 759
Huang, Y., Chen, B.-Q., Yuan, H.-B., et al. 2019, ApJS, 243, 7
Ivezić, Ž., Sesar, B., Jurić, M., et al. 2008, ApJ, 684, 287
Ivezić, Ž., Kahn, S. M., Tyson, J. A., et al. 2019, ApJ, 873, 111
Jurić, M., Ivezić, Ž., Brooks, A., et al. 2008, ApJ, 673, 864
Keller, S. C., Schmidt, B. P., Bessell, M. S., et al. 2007, PASA, 24, 1
Landolt, A. U. 1992, AJ, 104, 372
Landolt, A. U. 2009, AJ, 137, 4186
Landolt, A. U. 2013, AJ, 146, 131
Liu X. -W., et al., 2014, in Feltzing S., Zhao G., Walton N., Whitelock P., eds, Proc. IAU Symp. 298, Setting the scene for Gaia and LAMOST, Cambridge University Press, pp. 310-321, preprint (arXiv: 1306.5376)
Onken, C. A., Wolf, C., Bessell, M. S., et al. 2019, PASA, 36, e033 (DOI: 10.1017/pasa.2019.27)
Padmanabhan, N., Schlegel, D. J., Seljak, U., et al. 2007, MNRAS, 378, 852
Padmanabhan, N., Schlegel, D. J., Finkbeiner, D. P., et al. 2008, ApJ, 674, 1217
Pickles, A. J. 1998, PASP, 110, 863
Ramírez, I., & Meléndez, J. 2005, ApJ, 626, 465
Schlafly, E. F., Finkbeiner, D. P., Schlegel, D. J., et al. 2010, ApJ, 725, 1175
Schlegel, D. J., Finkbeiner, D. P., & Davis, M. 1998, ApJ, 500, 525
Steinmetz, M., Zwitter, T., Siebert, A., et al. 2006, AJ, 132, 1645
Stetson, P. B. 2000, PASP, 112, 925
Stubbs, C. W., & Tonry, J. L. 2006, ApJ, 646, 1436
Skrutskie, M. F., Cutri, R. M., Stiening, R., et al. 2006, AJ, 131, 1163
Tonry, J. L., Denneau, L., Flewelling, H., et al. 2018, ApJ, 867, 105
Wolf, C., Onken, C. A., Luvaul, L. C., et al. 2018, PASA, 35, e010 (DOI: 10.4225/41/593620ad5b574)
Wright, E. L., Eisenhardt, P. R. M., Mainzer, A. K., et al. 2010, AJ, 140, 1868
Yanny, B., Rockosi, C., Newberg, H. J., et al. 2009, AJ, 137, 4377
York, D. G., Adelman, J., Anderson, J. E., Jr., et al. 2000, AJ, 120, 1579
Yuan, H. B., & Liu, X. W. 2012, MNRAS, 425, 1763
Yuan, H. B., Liu, X. W., & Xiang, M. S. 2013, MNRAS, 430, 2188
Yuan, H., Liu, X., Xiang, M., et al. 2015, ApJ, 799, 133

Table A1
Magnitude offsets as a function of SFD $E(B-V)$

SFD $E(B-V)$ (mag)	Δu (mag)	Δv (mag)	Δg (mag)	Δr (mag)	Δi (mag)	Δz (mag)
$[0.000, 0.020]$	-0.0038	$+0.0000$	-0.0023	-0.0029	-0.0009	$+0.0015$
$[0.020, 0.040]$	$+0.0084$	$+0.0111$	-0.0014	-0.0019	$+0.0004$	$+0.0038$
$[0.040, 0.060]$	$+0.0294$	$+0.0281$	-0.0004	-0.0017	$+0.0018$	$+0.0068$
$[0.060, 0.080]$	$+0.0472$	$+0.0413$	$+0.0008$	-0.0007	$+0.0029$	$+0.0088$
$[0.080, 0.100]$	$+0.0701$	$+0.0560$	$+0.0022$	$+0.0005$	$+0.0038$	$+0.0105$
$[0.100, 0.120]$	$+0.0875$	$+0.0697$	$+0.0044$	$+0.0024$	$+0.0058$	$+0.0123$
$[0.120, 0.140]$	$+0.1068$	$+0.0838$	$+0.0059$	$+0.0044$	$+0.0071$	$+0.0140$
$[0.140, 0.160]$	$+0.1289$	$+0.0996$	$+0.0068$	$+0.0057$	$+0.0076$	$+0.0153$
$[0.160, 0.180]$	$+0.1464$	$+0.1126$	$+0.0084$	$+0.0077$	$+0.0091$	$+0.0166$
$[0.180, 0.200]$	$+0.1617$	$+0.1244$	$+0.0117$	$+0.0107$	$+0.0120$	$+0.0191$
$[0.200, 0.220]$	$+0.1751$	$+0.1334$	$+0.0136$	$+0.0119$	$+0.0144$	$+0.0208$
$[0.220, 0.240]$	$+0.1865$	$+0.1448$	$+0.0166$	$+0.0148$	$+0.0171$	$+0.0235$
$[0.240, 0.260]$	$+0.1970$	$+0.1530$	$+0.0187$	$+0.0170$	$+0.0203$	$+0.0267$
$[0.260, 0.280]$	$+0.2035$	$+0.1670$	$+0.0207$	$+0.0175$	$+0.0218$	$+0.0299$
$[0.280, 0.300]$	$+0.2126$	$+0.1790$	$+0.0222$	$+0.0180$	$+0.0244$	$+0.0319$
$[0.300, 0.350]$	$+0.2243$	$+0.1897$	$+0.0262$	$+0.0205$	$+0.0282$	$+0.0345$
$[0.350, 0.400]$	$+0.2305$	$+0.2095$	$+0.0296$	$+0.0219$	$+0.0303$	$+0.0394$
$[0.400, 0.500]$	$+0.2369$	$+0.2260$	$+0.0344$	$+0.0226$	$+0.0380$	$+0.0455$
$[0.500, 0.600]$	$+0.2624$	$+0.2517$	$+0.0402$	$+0.0218$	$+0.0487$	$+0.0506$
$[0.600, 0.800]$	$+0.2856$	$+0.2809$	$+0.0267$	$+0.0113$	$+0.0316$	$+0.0436$
$[0.800, 1.000]$	$+0.2901$	$+0.3034$	$+0.0147$	$+0.0004$	$+0.0022$	$+0.0334$
$[1.000, 1.500]$	$+0.2645$	$+0.2437$	$+0.0083$	$+0.0075$	$+0.0070$	$+0.0202$
$[1.500, 2.500]$	$+0.2242$	$+0.1961$	$+0.0054$	$+0.0018$	$+0.0089$	$+0.0195$

Table A2
Fit coefficients for the magnitude differences as a function of δ for uv bands and b for $griz$ bands

ΔX (mag)	a_0	a_1	a_2	a_3	a_4	a_5	Note
u	5.73×10^{-4}	1.54×10^{-3}	1.08×10^{-5}	-1.04×10^{-6}	-2.32×10^{-8}	-1.64×10^{-10}	$\alpha > 300°$
	-1.96×10^{-3}	3.44×10^{-4}	-3.69×10^{-6}	-7.53×10^{-7}	-1.50×10^{-8}	-1.01×10^{-10}	$\alpha < 180°$ or $260° < \alpha < 300°$
	-2.02×10^{-2}	3.00×10^{-3}	2.47×10^{-4}	6.88×10^{-6}	8.67×10^{-8}	3.94×10^{-10}	$\alpha < 180°$
v	-9.97×10^{-3}	-3.62×10^{-4}	-4.61×10^{-5}	-1.28×10^{-6}	-9.69×10^{-9}	–	$\alpha > 300°$
	-4.16×10^{-3}	-2.34×10^{-4}	9.89×10^{-6}	3.20×10^{-7}	1.94×10^{-9}	–	$\alpha < 180°$ or $260° < \alpha < 300°$
	-1.73×10^{-2}	1.09×10^{-3}	8.29×10^{-5}	1.22×10^{-6}	4.86×10^{-9}	–	$\alpha < 180°$
g	1.36	-1.37	-3.51×10^{-3}	-9.39×10^{-5}	–	–	$(180° \leq l < 330°)$ and $b > 0°$
	3.35	-3.36	-4.07×10^{-3}	-6.23×10^{-4}	–	–	$(l \leq 180°$ or $l > 330°)$ and $b > 0°$
	1.10×10^{-2}	-3.16×10^{-2}	-4.62×10^{-1}	9.82×10^{-5}	–	–	$(180° \leq l < 330°)$ and $b < 0°$
	8.70	-8.71	-5.46×10^{-4}	3.73×10^{-5}	–	–	$(l \leq 180°$ or $l > 330°)$ and $b < 0°$
r	1.18	-1.19	-3.71×10^{-3}	-3.28×10^{-5}	–	–	$(180° \leq l < 330°)$ and $b > 0°$
	3.01×10	-3.01×10	-3.68×10^{-4}	-4.08×10^{-4}	–	–	$(l \leq 180°$ or $l > 330°)$ and $b > 0°$
	9.08	-9.09	-5.57×10^{-4}	1.52×10^{-4}	–	–	$(180° \leq l < 330°)$ and $b < 0°$
	8.66×10	-8.66×10	-9.80×10^{-5}	1.04×10^{-4}	–	–	$(l \leq 180°$ or $l > 330°)$ and $b < 0°$
i	8.64×10^{-1}	-8.76×10^{-1}	-6.83×10^{-3}	-1.97×10^{-4}	–	–	$(180° \leq l < 330°)$ and $b > 0°$
	7.93×10^{-2}	-1.08×10^{-1}	-2.44×10^{-1}	-6.98×10^{-4}	–	–	$(l \leq 180°$ or $l > 330°)$ and $b > 0°$
	4.18×10^{-3}	-2.56×10^{-2}	$-9.16 \times^{-1}$	6.55×10^{-5}	–	–	$(180° \leq l < 330°)$ and $b < 0°$
	1.07	-1.10	-9.62×10^{-3}	2.77×10^{-4}	–	–	$(l \leq 180°$ or $l > 330°)$ and $b < 0°$
z	1.31×10^{-2}	-1.78×10^{-2}	-3.29×10^{-1}	-2.16×10^{-4}	–	–	$(180° \leq l < 330°)$ and $b > 0°$
	2.83×10^{-2}	-4.44×10^{-2}	-4.72×10^{-1}	-5.40×10^{-4}	–	–	$(l \leq 180°$ or $l > 330°)$ and $b > 0°$
	1.95	-1.95	-1.42×10^{-3}	1.69×10^{-4}	–	–	$(180° \leq l < 330°)$ and $b < 0°$
	1.46×10^{-2}	-2.96×10^{-2}	-4.52×10^{-1}	1.97×10^{-4}	–	–	$(l \leq 180°$ or $l > 330°)$ and $b < 0°$